buildings

MDPI

Article

Modified Constitutive Models and Mechanical Properties of GFRP after High-Temperature Cooling

Junjie Wu [1,2] and Chuntao Zhang [1,2,3,*]

[1] Shock and Vibration of Engineering Materials and Structures Key Laboratory of Sichuan Province, Mianyang 621010, China; wujunjie19981228@163.com
[2] School of Civil Engineering and Architecture, Southwest University of Science and Technology, Mianyang 621010, China
[3] Department of Mechanical Engineering, University of Houston, Houston, TX 77204, USA
* Correspondence: chuntaozhang@swust.edu.cn

Abstract: Many materials are highly sensitive to temperature, and the study of the fire resistance of materials is one of the important research directions, which includes the study of the fire resistance of fiber-reinforced polymer (FRP) composites, but the cooling mode on the change of FRP mechanical properties after high temperature has not been investigated. This study analyzes the mechanical properties of GFRP under various cooling methods after exposure to high temperatures. The tensile strength of GFRP was evaluated through water cooling, firefighting foam cooling, and air cooling within the temperature range of 20–300 °C. Damage modes were investigated at different target temperatures. The results indicate that the tensile strength of air-cooled GFRP is the highest, whereas water cooling yields the lowest retention rate. It indicates that the FRP temperature decreases slowly under air cooling and the better recovery of the damage within the resin matrix, while under water cooling, the damage at the fiber/resin interface is exacerbated because of the high exposed temperature and the water, resulting in a reduction in the strength of GFRP. Between 20 and 150 °C, GFRP essentially recovers its mechanical properties after cooling, with a residual tensile strength factor exceeding 0.9. In the range of 150–250 °C, GFRP exhibits a graded decline in strength. At 300 °C, GFRP loses certain mechanical properties after cooling, with a residual tensile strength factor below 0.1. Furthermore, the analysis of experimental results led to the modification of the Johnson–Cook constitutive model, proposing a model for GFRP under three cooling methods. Additionally, a predictive model for the elastic modulus of GFRP after high-temperature cooling was derived, showing agreement with experimental results.

Keywords: glass fiber-reinforced polymer (GFRP); cooling methods; mechanical properties; modified constitutive model

Citation: Wu, J.; Zhang, C. Modified Constitutive Models and Mechanical Properties of GFRP after High-Temperature Cooling. *Buildings* **2024**, *14*, 439. https://doi.org/10.3390/buildings14020439

Academic Editor: Cedric Payan

Received: 27 December 2023
Revised: 20 January 2024
Accepted: 26 January 2024
Published: 5 February 2024

1. Introduction

Fiber-reinforced polymer (FRP) composites, known for their lightweight and high strength, offer excellent corrosion resistance and specific strength. They find diverse applications in aerospace, military, civil construction, and infrastructure projects, serving as cost-effective alternatives to traditional steel components [1–4]. Understanding the mechanical behavior of FRP composites at elevated temperatures is crucial for both civil and military applications [5,6]. In addition to being cheaper than AFRP and CFRP, GFRP has better bonding performance and mature technology. As a result, it is used in large-scale applications in various fields. So this paper conducts experimental research using GFRP. These composites, comprised of glass fibers, carbon fibers, and a resin matrix formed through processes like winding, molding, or pultrusion, are particularly sensitive to temperature variations, with the resin component being a key influencing factor.

The resin matrix in FRP commonly consists of thermosetting and thermoplastic resins, both of which are prone to softening at elevated temperatures. As the temperature rises, the

matrix undergoes transitions from a glassy to a leathery, rubbery, and eventually decomposed state, leading to a notable decline in FRP's mechanical properties [7,8]. In addition, the tensile strength of FRP decreases significantly with increasing exposed temperature and time [9]. Experimental and theoretical support is essential to ascertaining the post-fire mechanical behavior of FRP, a critical consideration for structures seeking to regain functionality after fire incidents. Consequently, investigating the mechanical properties of FRP at high temperatures becomes imperative.

Exploration into the mechanical properties of FRP at elevated temperatures stands as a pivotal focus within FRP material research. This exploration encompasses three primary directions: the mechanical behavior of FRP at high temperatures [6,10–14], the bond strength of FRP reinforcement and concrete under high temperatures [15–20], and the effects of high temperatures on FRP reinforcing and restraining components [21–25]. Numerous researchers have delved into this subject, utilizing experimental, numerical, and analytical approaches. For instance, Zike Wang [9] presents an investigation on the durability of basalt- and glass-fiber-reinforced polymer bars exposed to an SWSSC environment under different sustained stress levels. It was experimentally obtained that the tensile strength of BFRP and GFRP decreased significantly under the combined effect of sustained stress and exposure temperature. Gang Wu [26] investigated the tensile properties of BFRP bars under four environments: alkaline solution, salt solution, acid solution, and de-ionized water at 25, 40, and 55 °C. The results showed that the exposure temperature and environmental corrosion can damage the fiber/resin interface, resulting in a significant decrease in the tensile strength of BFRP bars. H. Wang et al. [27] conducted dynamic and quasi-static compressive tests on a ceramicized polymer composite, revealing a substantial decrease in compressive strength with increasing temperature. Khaneghahi MH et al. [28] explored the impact of intumescent paint on the mechanical properties of FRP at various temperatures, observing a significant inhibitory effect on the decrease in tensile strength. C. Wang [29] investigated the mechanical properties of FRP as internal reinforcement in concrete structures at high temperatures, noting variations in performance. Despite these valuable insights, existing research predominantly focuses on the mechanical properties of FRP materials at elevated temperatures, leaving a notable gap in the exploration of their behavior after high-temperature cooling—an essential consideration for preserving FRP performance after exposure to elevated temperatures.

By investigating the effects of different cooling methods on the mechanical properties of GFRP after high temperature, the aim of this study is to provide the best fire extinguishing method for GFRP materials after exposure to fire, and to establish the constitutive model of GFRP under different cooling methods after high temperature. This is crucial for the application of GFRP in practical engineering and provides a basis for the reliability assessment of thermal protection structures in extreme environments. In addition to this, providing the failure range of GFRP's mechanical properties after cooling will facilitate the safety assessment of the building.

2. Materials and Methods

2.1. Specimen Design

The Glass Fiber Reinforced Polymer (GFRP), a flat strip composed of unsaturated polyester resin and glass fibers, was chosen for this test. The design approach for the layering structure of GFRP is unidirectional layering. The thermosetting temperature of this resin is approximately 90 °C. According to GB/T 1447-2005 [30], the dimensions and configuration of the GFRP are depicted in Figure 1. With a thickness of 3.7 mm and a fiber volume fraction of 62%, the glass fibers are predominantly aligned along the axial direction of the plate. Table 1 presents the essential mechanical properties of the GFRP.

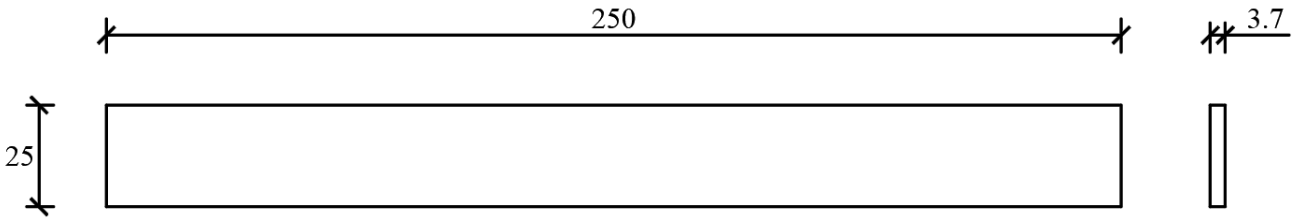

Figure 1. Dimensions of the test specimen (mm).

Table 1. Mechanical Properties of GFRP.

Specimen Labels	Tensile Strength f_u/MPa	Modulus of Elasticity E/GPa	Elongation δ/%
1	427.89	37.05	12.05
2	563.31	39.16	14.33
3	467.92	38.15	12.51
Average	486.37	38.12	12.96
Standard Deviation	56.80	0.86	0.98

2.2. Test Procedures

To investigate the impact of different cooling methods on GFRP after exposure to high temperatures, the test involved five target temperatures and 48 specimens. Three specimens were tested at each target temperature using various cooling methods, and an additional three specimens were kept at ambient temperature as a control group. The high-temperature setting utilized a box-shaped resistance furnace (SX2-4-10 type) which is illustrated in Figure 2a, with target temperatures set at 100 °C, 150 °C, 200 °C, 250 °C, and 300 °C. After reaching the target temperature, the specimens were left for a one-hour constant temperature phase, according to GB/T 38515-2020 [31]. Subsequently, cooling was performed using water, firefighting foam, and the natural cooling method. The entire process, including heating, insulation, and cooling under different target temperatures, is illustrated in Figure 3. After cooling to ambient temperature, a strain gauge was affixed to the center of each specimen to measure the GFRP strain. A static tensile test, according to GB/T 1447-2005 [30], involved controlling tensile loading by displacement with a loading rate of 1 mm/min until specimen fracture. The EMT504D electronic universal testing machine (Figure 2b) is manufactured in Shenzhen Wance Testing Equipment Co., Ltd., Shenzhen, China, and the load cell used is S-TYPE LOAD CELLS, which facilitated the static tensile test. The comparison and analysis of test results under different temperature conditions, including the stress–strain relationship curve of GFRP and related mechanical property parameters, were conducted to assess the influence of elevated temperatures and cooling methods.

(**a**) Electric furnace

(**b**) ETM series electronic universal testing machine

Figure 2. Test equipment.

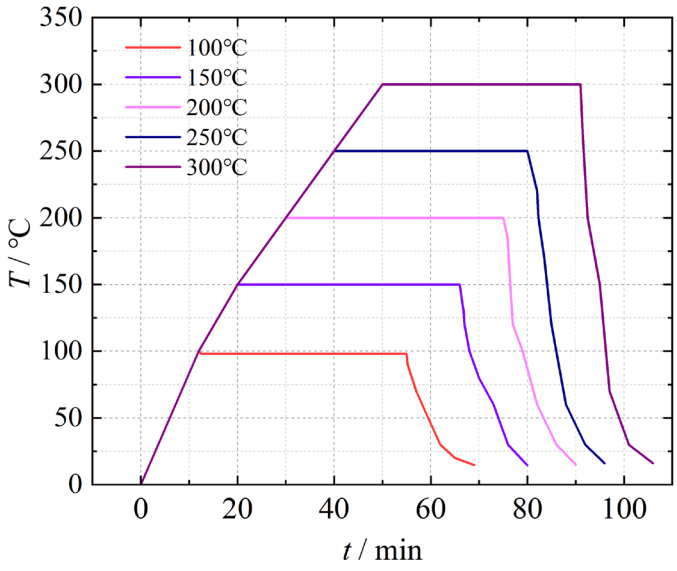

Figure 3. Temperature–time curves.

3. Test Results

3.1. Experimental Phenomena

3.1.1. Surface Characteristics

The surface color variations of the test specimens after exposure to high temperatures are illustrated in Figure 4. It can be seen that the cooling methods slightly affect the characteristics of the specimen. Under natural conditions, the GFRP surface exhibited a yellow hue. As the temperature increased, heating at 100 °C, 150 °C, and 200 °C led to a gradual deepening of the color, transitioning from a slightly blackened appearance to localized brown and eventually to brown. At temperatures approximately between

65 °C and 120 °C, the glass fiber reinforced plastic (GFRP) material undergoes its first glass transition, causing the material's resin to shift from a glassy state to a rubbery state [32]. At 250 °C, the surface turned charcoal-black, and the outer protective layer began to partially detach. Upon reaching 300 °C, the entire surface became charcoal-black due to the carbonization of the outer protective layer, which completely detached from the structural layer of the GFRP.

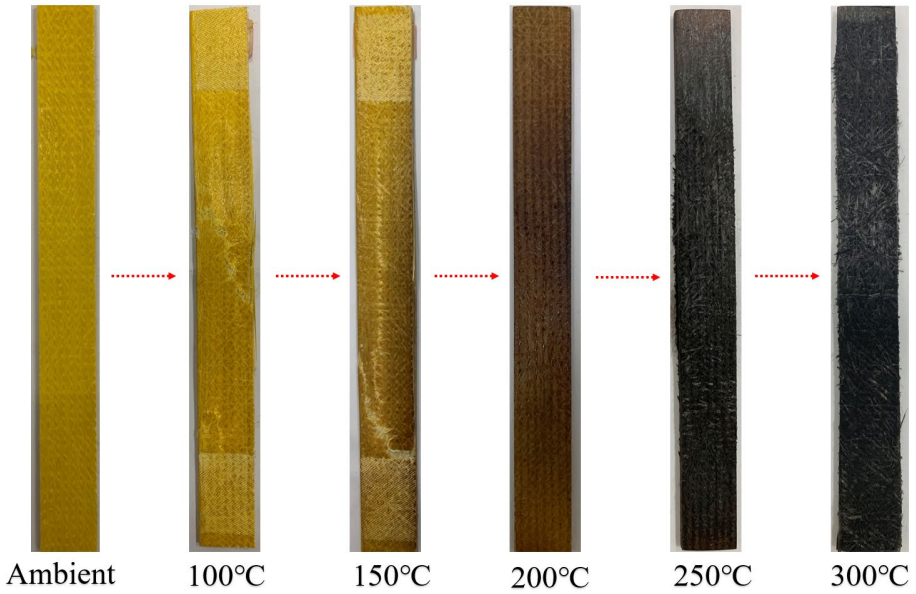

(**a**) Air cooling

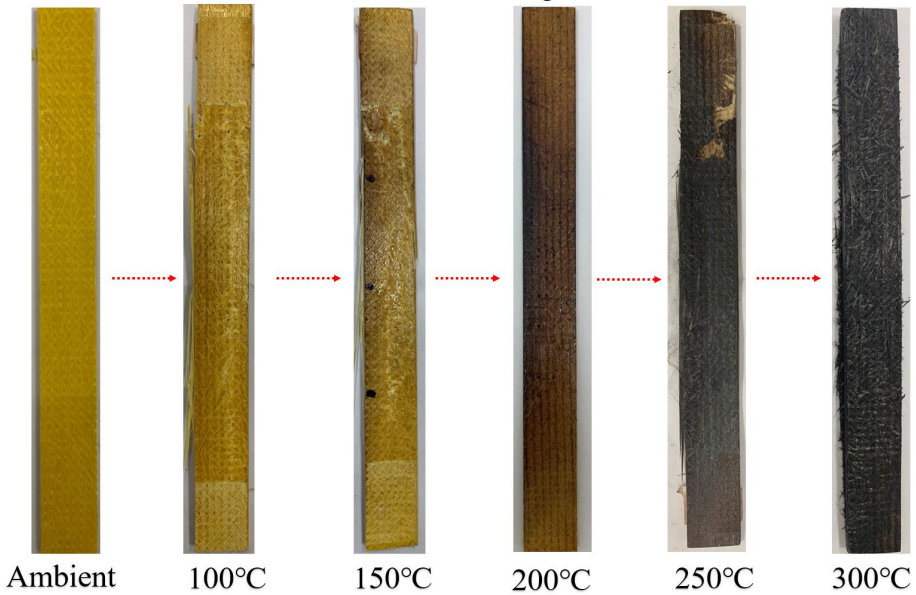

(**b**) Firefighting foam cooling

Figure 4. *Cont.*

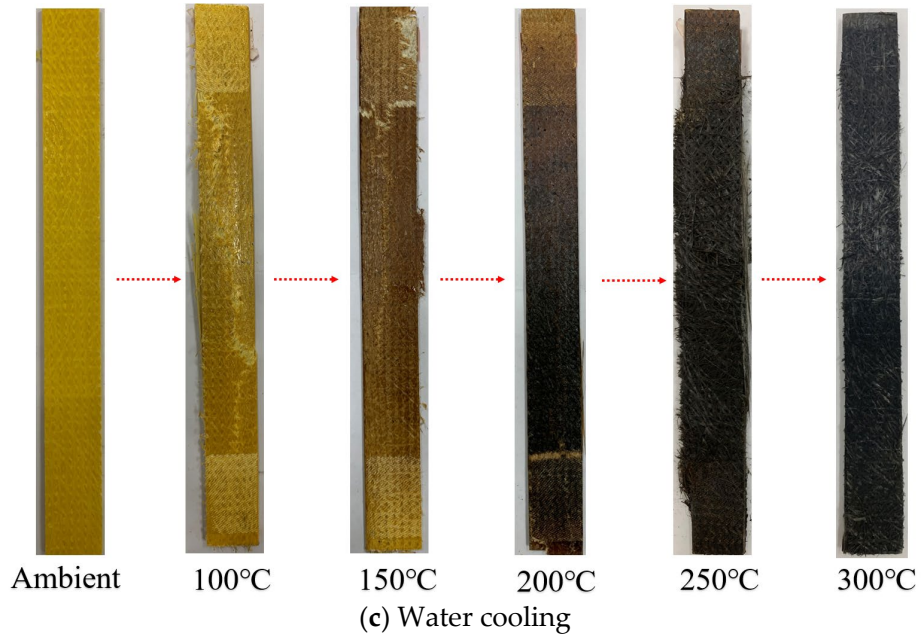

Figure 4. Surface characteristics.

3.1.2. Failure Mode

The tensile failure characteristics of Glass Fiber Reinforced Polymer (GFRP) after high-temperature cooling at various target temperatures are presented in Figures 5–7. Observing the figures reveals distinct stage differences in failure characteristics corresponding to changes in temperature. As the temperature increased from ambient to 100 °C, 150 °C, and 200 °C, the fracture patterns exhibited notable variations. Initially, there was resin adhesion between the fibers, indicating integral destruction of the glass fibers and resin with a concentrated fiber distribution. As the temperature continued to rise, the fibers transitioned gradually into a diffuse filamentous state.

At ambient temperature and 100 °C, GFRP experienced cracking along axial extension, followed by destruction after the fiber bundles burst out. At 100 °C, the three cooling methods showed no significant impact on GFRP failure characteristics, with fiber bonding similar to that at ambient temperature, suggesting that the coordinated working ability of the fibers and resin remained relatively unchanged. At 150 °C and 200 °C, GFRP exhibited cracks extending from the axial center, while the final fracture leaned toward the end of the fixture. In comparison, natural cooling resulted in more dispersed fibers than water cooling and foam cooling, indicating that the latter two methods played a role in the recovery of resin after thermal decomposition.

Simultaneously, with the temperature increase, the flocculent material at the GFRP fracture gradually increased. At 250 °C, the fibers dispersed after failure, indicating that a large portion of the resin in the specimen could not be recovered after cooling. Notably, fiber bundle dispersion was relatively low under natural cooling. When the temperature reached 300 °C, fibers at the fracture of GFRP, cooled by all three methods, exhibited a diffuse filamentous state, indicating de-bonding and complete carbonization of the GFRP. Consequently, recovery through cooling was not possible at this temperature.

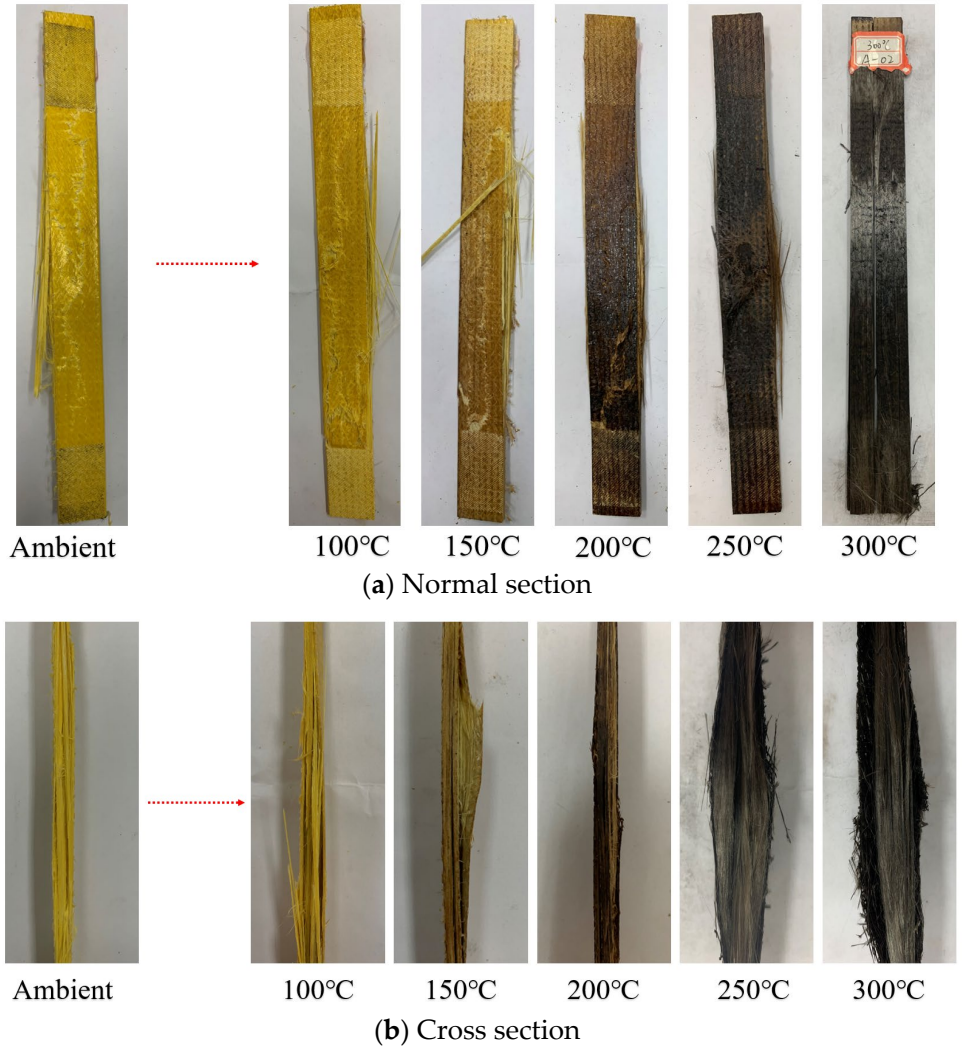

Figure 5. Air cooling.

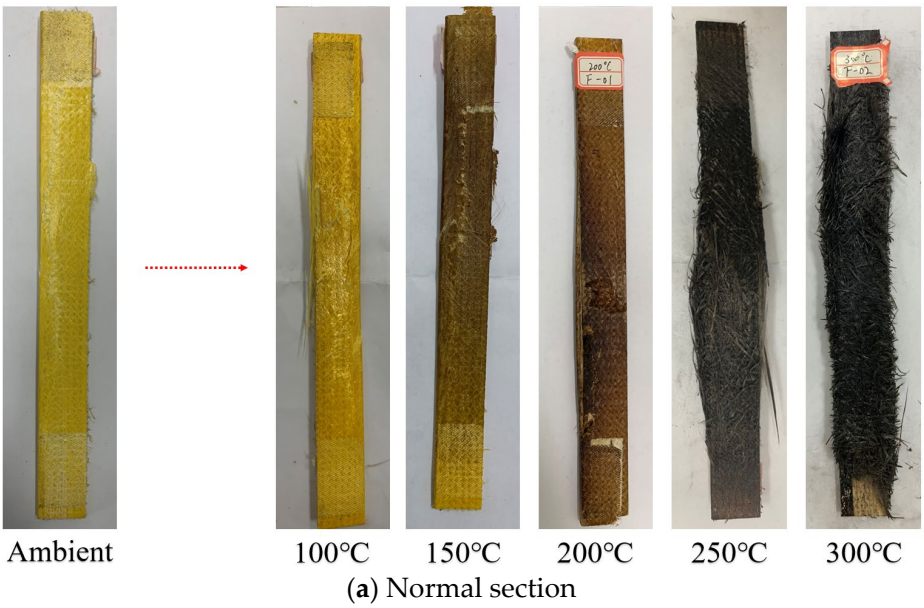

Figure 6. *Cont.*

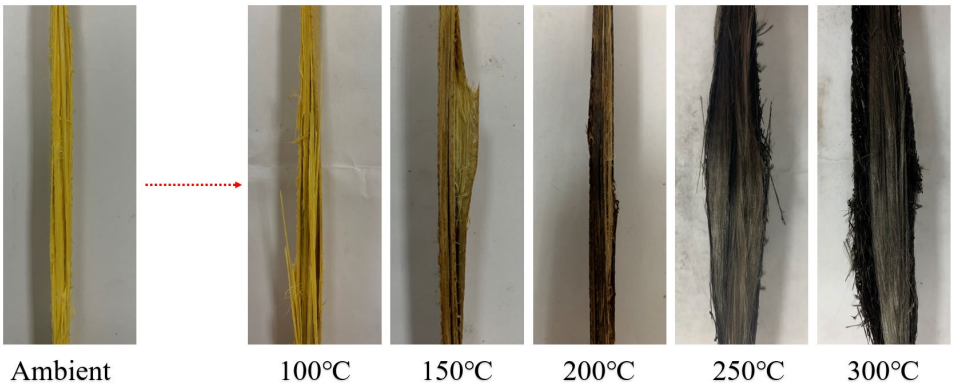

Figure 6. Firefighting foam cooling.

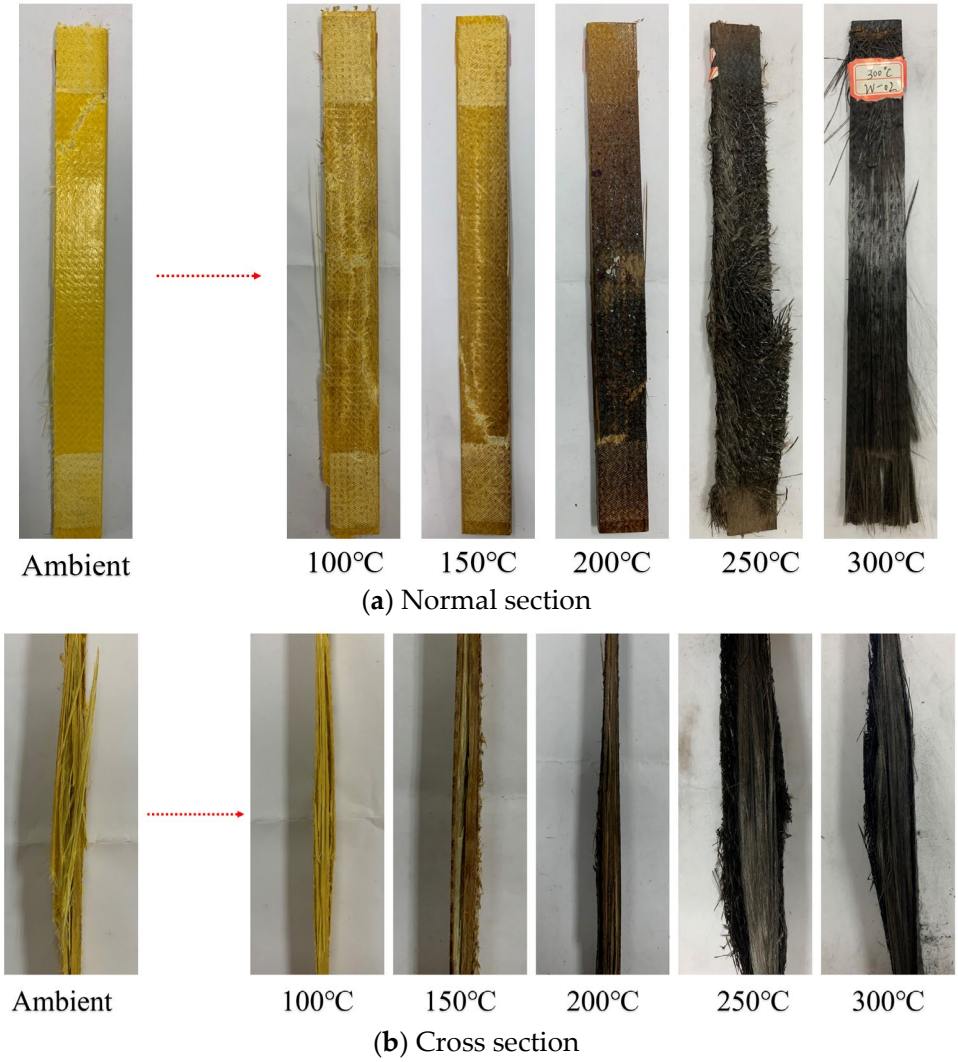

Figure 7. Water cooling.

3.2. Mechanical Properties

3.2.1. Tensile Strength

The maximum stress value reached when materials undergo damage under the action of force is termed tensile strength. Table 2 illustrates the tensile strength and residual factors of materials after high-temperature cooling at various target temperatures.

At 100 °C, compared to ambient temperature (σ_{max} = 486.38 MPa), the tensile strength under air cooling and foam cooling specimens increased, while water-cooled specimens (σ_{max} = 457.30 MPa) exhibited a decrease. At 100 °C, the resin matrix is undergoing a transition from a glassy state to a rubbery state [32]. This suggests that a reduction reaction enhanced the strength of materials after high-temperature cooling at the target temperature, and air cooling was more conducive to preserving material strength by allowing the reduction reaction to proceed more effectively.

At 150 °C, the residual factor of tensile strength under air cooling was 1.0, indicating effective restoration of material strength. Water and foam cooling exhibited residual factors of 0.90 and 0.83, respectively, indicating a decrease in strength when the temperature exceeded 150 °C. However, under air cooling, the strength exhibited a decreasing trend when the temperature surpassed 200 °C, suggesting that air cooling remained more beneficial for preserving material strength.

At 250 °C, tensile strength significantly decreased, signifying a sharp decline in the resin's bearing capacity due to thermal decomposition, resulting in permanent damage even after cooling. At 300 °C, a change in the damage mode occurred, with the stress slowly decreasing after reaching tensile strength, revealing resin carbonization. Despite cooling, the material lost load-bearing capacity after 300 °C. The strength retention rates for the three cooling methods at the same target temperature followed the order: air cooling > foam cooling > water cooling. After reaching 250 °C, none of the cooling methods could restore the strength.

It indicates that at temperatures above 250 °C, the degree of glass transition of the resin is more pronounced at high temperature. The destruction of the fiber/resin interface is aggravated by the combination of a higher exposure temperature and water cooling. Eventually, the glass fibers debond from the resin, resulting in a significant decrease in the tensile strength of GFRP [33].

Figure 8 illustrates the fitted line between tensile strength and high temperature, showcasing a decrease in the tensile strength of GFRP tubes as temperatures increased. The response of the tensile strength–temperature ratio presented a curvature. The curvatures of air cooling and foam cooling were similar, while water cooling exhibited a gentler change. Regression analysis of the experimental results yielded the following expressions for GFRP tubes:

Air cooling:

$$y_a = -1.07 \times 10^{-2} x^2 + 1.82x + 451.82 \quad (1)$$

Fire foam cooling:

$$y_f = -1.03 \times 10^{-2} x^2 + 1.57x + 463.47 \quad (2)$$

Water cooling:

$$y_w = -6.20 \times 10^{-3} x^2 + 0.30x + 488.37 \quad (3)$$

The reliability coefficients (R^2) for the fit curve under air cooling, foam cooling, and water cooling are 0.941, 0.917, and 0.921, respectively, indicating a favorable matching effect. This implies that the experiment exhibits minimal data dispersion, validating the credibility and accuracy of the collected data.

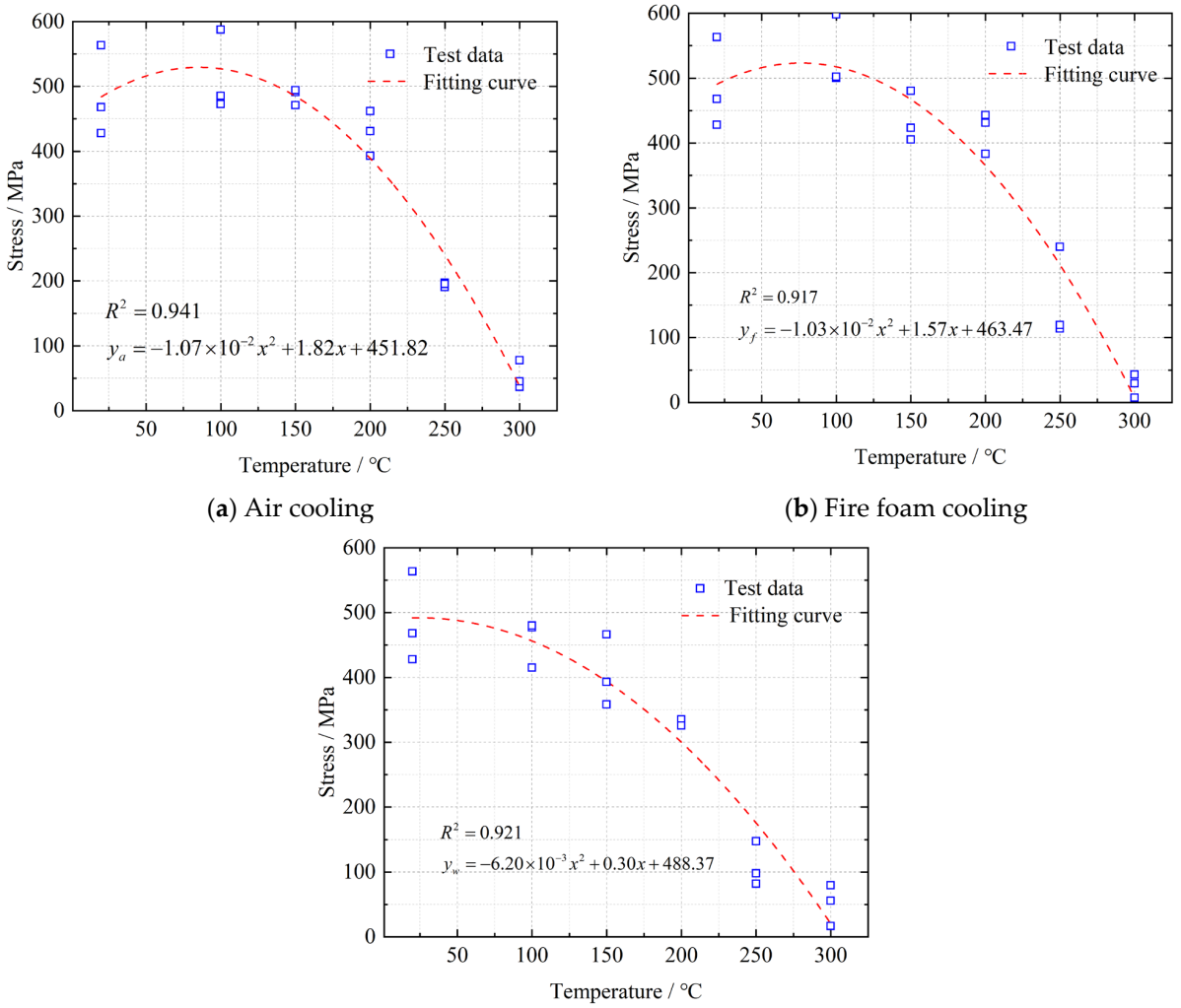

(**a**) Air cooling (**b**) Fire foam cooling

(**c**) Water cooling

Figure 8. Ultimate strength of GFRP composites after high-temperature cooling.

Table 2. Tensile strength and residual factors of GFRP composites after high-temperature cooling.

Cooling Methods	Temperature/°C	Tensile Strength (MPa)				Residual Factor (σ_T/σ_{20})			
		Group-1	Group-2	Group-3	Average	Group-1	Group-2	Group-3	Average
Air Cooling	Ambient	427.89	563.35	467.89	486.38	0.88	1.16	0.96	1.00
	100	587.68	485.30	472.76	515.24	1.21	1.00	0.97	1.06
	150	490.92	470.92	493.95	485.26	1.01	0.97	1.02	1.00
	200	461.95	431.03	392.76	428.58	0.95	0.89	0.81	0.88
	250	197.30	190.38	195.24	194.31	0.41	0.39	0.40	0.40
	300	77.73	36.54	45.19	53.15	0.16	0.08	0.09	0.11
Fire Foam Cooling	Ambient	427.89	563.35	467.89	486.38	0.88	1.16	0.96	1.00
	100	598.05	499.89	502.16	533.37	1.23	1.03	1.03	1.10
	150	405.41	423.35	480.32	436.36	0.83	0.87	0.99	0.90
	200	443.03	383.24	431.14	419.14	0.91	0.79	0.89	0.86
	250	113.84	119.46	239.89	157.73	0.23	0.25	0.49	0.32
	300	7.14	42.92	29.30	26.45	0.01	0.09	0.06	0.05
Water Cooling	Ambient	427.89	563.35	467.89	486.38	0.88	1.16	0.96	1.00
	100	415.03	477.08	479.78	457.30	0.85	0.98	0.99	0.94
	150	466.38	358.38	392.86	405.87	0.96	0.74	0.81	0.83
	200	326.05	335.03	325.51	328.86	0.67	0.69	0.67	0.68
	250	97.62	81.84	147.24	108.90	0.20	0.17	0.30	0.22
	300	16.43	55.78	79.46	50.56	0.03	0.11	0.16	0.10

3.2.2. Modulus of Elasticity

The experimental findings presented in Table 3 reveal that the elastic modulus of the material under natural and foam cooling at the target temperature of 100 °C experienced a noticeable increase. Specifically, the elastic modulus showed a 20% enhancement under air cooling, indicating a strengthening process. There was no significant difference in the elastic modulus at the target temperatures of 100 °C and 150 °C, and the change in the residual factor of the elastic modulus was within 5%. This suggests that the alteration in the elastic modulus after air cooling within this temperature range is relatively minor, implying no distinct impact on the collaborative working performance of the resin and glass fibers.

Table 3. Elastic moduli and residual factors of GFRP composites after high-temperature cooling.

Cooling Methods	Temperature/°C	Elastic Modulus (GPa)				Residual Factor (E_T/E_{20})			
		Group-1	Group-2	Group-3	Average	Group-1	Group-2	Group-3	Average
Air Cooling	Ambient	37.05	39.16	38.15	38.12	0.97	1.03	1.00	1.00
	100	42.37	54.33	39.96	40.06	1.11	1.42	1.04	1.19
	150	41.78	38.40	39.61	39.93	1.09	1.01	1.03	1.04
	200	43.14	39.39	34.44	38.99	1.13	1.03	0.90	1.02
	250	32.53	28.20	28.97	29.90	0.85	0.74	0.75	0.78
	300	11.26	3.26	10.29	8.27	0.30	0.08	0.26	0.21
Fire Foam Cooling	Ambient	37.05	39.16	38.15	38.12	0.97	1.03	1.00	1.00
	100	41.22	41.74	37.97	40.31	1.08	1.09	0.99	1.05
	150	38.12	36.83	36.21	37.05	0.99	0.97	0.94	0.97
	200	33.70	36.41	38.32	36.15	0.88	0.95	1.00	0.94
	250	17.91	27.87	28.89	24.89	0.46	0.73	0.75	0.65
	300	2.08	9.39	11.40	7.62	0.05	0.24	0.29	0.19
Water Cooling	Ambient	37.05	39.16	38.15	38.12	0.97	1.03	1.00	1.00
	100	36.80	37.98	37.88	37.55	0.96	0.99	0.99	0.98
	150	39.54	39.33	37.12	38.66	1.04	1.03	0.97	1.01
	200	36.17	36.25	32.68	35.03	0.94	0.95	0.85	0.91
	250	13.67	15.05	16.50	15.08	0.35	0.39	0.43	0.39
	300	5.21	1.28	10.46	5.65	0.14	0.03	0.27	0.15

However, after reaching 250 °C, the elastic modulus exhibited a decline, with a notable 60% reduction under water cooling. This decline could be attributed to the fact that the structure of the unsaturated polyester resin experienced significant defects under water cooling. At 300 °C, the residual factor was 20% of the initial elastic modulus under all three cooling methods, and cooling was incapable of restoring the working abilities of the materials. Comparing with the average reduction in about 30% in tensile modulus under high-temperature conditions at 100 °C [34], it can be observed that the tensile modulus of GFRP tends to recover to some extent after cooling.

3.2.3. Ultimate Strain

Table 4 lists the tensile strength and the residual factor of the GFRP composites after high-temperature cooling, which indicated that in the range of 100 °C–300 °C, the tensile strength tends to decrease as the temperature increases. It is worth noting that the tensile strength of foam cooling is generally higher than that of the other two cooling methods, which could be attributed to the fact that foam cooling alters to some extent the bonding effects of the unsaturated polyester and the fiber material, which led to the mass increment of ductility. At 100 °C, the residual factors of the materials in natural and foam cooling are 1.01 and 1.03, respectively, indicating that the material is strengthened to a certain degree. The decrease in tensile strength is greater with water cooling than with other cooling methods, which may be due to defects in the redox process of unsaturated polyester, causing a decrease in the tensile strength of the materials.

Table 4. Ultimate strain and residual factors of GFRP composites after high-temperature cooling.

Cooling Methods	Temperature/°C	Ultimate Strain (%)				Residual Factor ($\varepsilon_T/\varepsilon_{20}$)			
		Group-1	Group-2	Group-3	Average	Group-1	Group-2	Group-3	Average
Air Cooling	Ambient	12.05	14.33	12.51	12.96	0.93	1.11	0.97	1.00
	100	14.31	13.54	11.28	13.04	1.10	1.04	0.87	1.01
	150	11.28	12.01	12.31	11.87	0.87	0.93	0.95	0.92
	200	11.52	11.40	9.80	10.90	0.89	0.88	0.76	0.84
	250	7.69	6.60	7.30	7.20	0.59	0.51	0.56	0.56
	300	6.42	15.35	4.16	8.64	0.50	1.18	0.32	0.67
Fire Foam Cooling	Ambient	12.05	14.33	12.51	12.96	0.93	1.11	0.97	1.00
	100	14.91	13.10	12.01	13.34	1.15	1.01	0.93	1.03
	150	10.14	10.57	11.87	10.86	0.78	0.82	0.92	0.84
	200	11.74	10.46	11.79	11.33	0.91	0.81	0.91	0.87
	250	8.02	6.38	9.80	8.06	0.62	0.49	0.76	0.62
	300	1.85	4.27	14.89	7.03	0.14	0.33	1.15	0.54
Water Cooling	Ambient	12.05	14.33	12.51	12.96	0.93	1.11	0.97	1.00
	100	10.71	12.31	11.81	11.61	0.83	0.95	0.91	0.90
	150	12.07	8.99	10.21	10.42	0.93	0.69	0.79	0.80
	200	8.89	9.31	9.72	9.31	0.69	0.72	0.75	0.72
	250	8.00	5.03	5.88	6.30	0.62	0.39	0.45	0.49
	300	2.81	11.65	5.92	6.79	0.22	0.90	0.46	0.52

3.3. Stress–Strain Curves

Figure 9 depicts the stress–strain curves of GFRP after water, foam, and air cooling at different target temperatures, revealing a brittle damage pattern in the materials. Examining the stress–strain curve of air cooling, it is evident that the tensile strength decreases with rising temperature. Before material destruction, the curve slopes linearly at ambient temperatures of 100 °C, 150 °C, and 200 °C, showing no significant differences. The tensile strength and ultimate strain at the target temperatures of 100 °C and 150 °C are similar, indicating that within the range of 100 °C to 150 °C, there is no notable impact on the coordinated working performance of the resin and glass fibers. However, at 250 °C, the tensile strength significantly drops as only the fiber can withstand the load, leading to thermal decomposition of the resin, which cannot be restored to its working performance after air cooling. At 300 °C, the damage mode changes, with the stress reaching its maximum value and then slowly declining, signifying that the materials have essentially lost their working abilities. Under this temperature condition, the stress–strain curve of the specimen after cooling exhibits significant plastic deformation. Based on the failure characteristics of the specimens, it is concluded that due to the higher exposure temperature, the resin is completely damaged, and only the fibers are in working condition, with the fibers in a divergent state. This results in significant plastic deformation.

Analyzing the strength–strain curve of foam cooling, it is evident that, compared to air cooling at the same temperature, the ultimate strain at 150 °C decreases and is even lower than that at 200 °C. This implies that the internal resin structure of GFRP undergoes changes after air cooling at this temperature, resulting in defects and a reduction in ultimate strain. The damage mode is similar to the air cooling curve under corresponding temperatures at 250 °C and 300 °C, with no significant differences. The cooling mode has a minimal effect on the materials at these temperatures. The strength–strain curves for water cooling show that the tensile strength at each target temperature is lower than those for natural and foam cooling. At 250 °C, the slope of GFRP decreases significantly after water cooling, lower than that of natural and foam cooling under the same target temperature. This is attributed to the weaker retention of strength under water cooling compared to the other two methods. The contact between the materials and water at high temperatures alters the resin structure, leading to defects and a reduction in strength. The materials exhibit plasticity damage at 250 °C and 300 °C after water cooling, resulting in a loss of their bearing capacities.

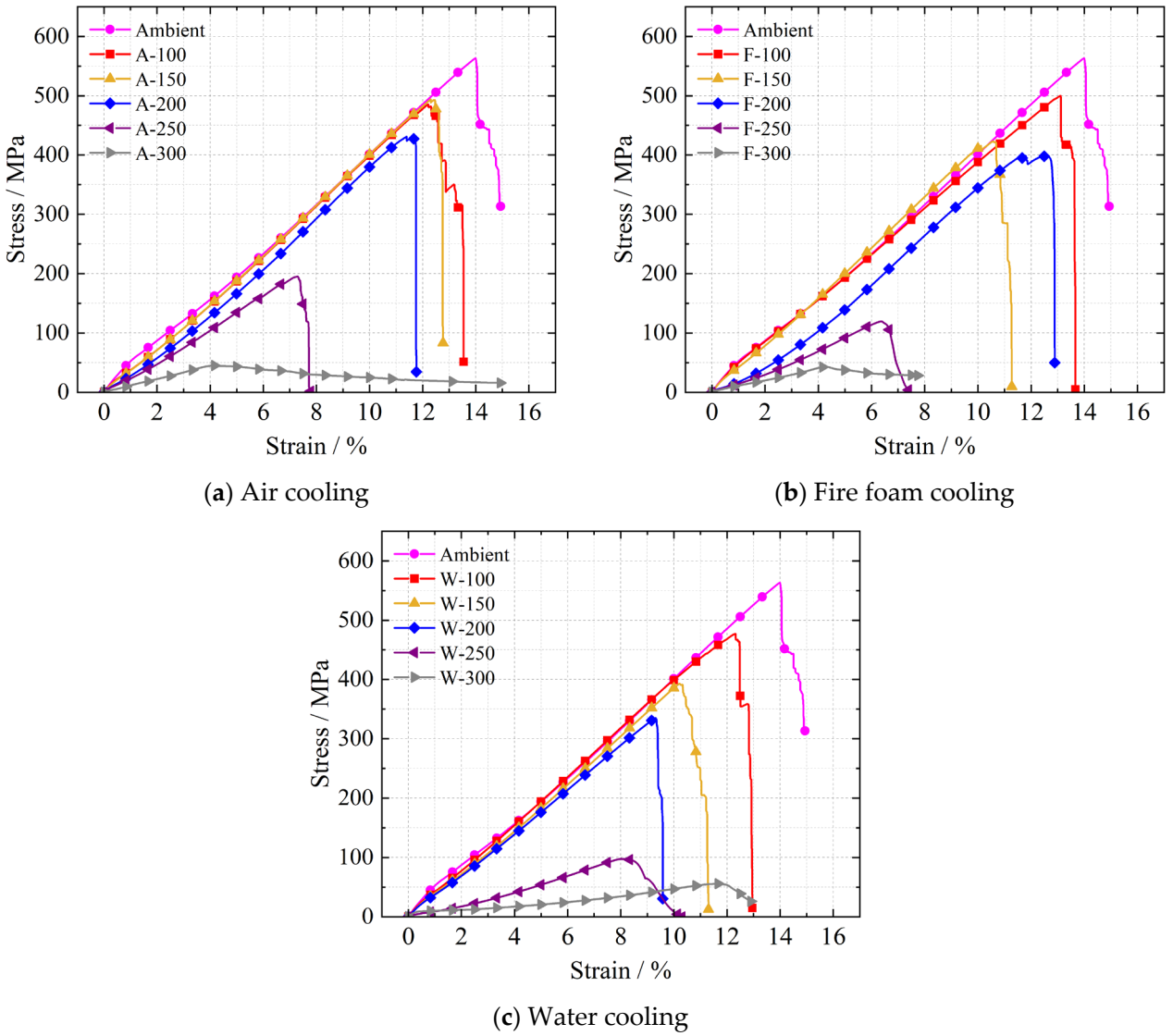

Figure 9. The stress–strain curve of GFRP after high-temperature cooling.

4. Theoretical Analysis

4.1. The T-E Model

To accurately determine the variation in the elastic modulus of GFRP after three cooling methods under different temperatures, the test was conducted using both an extensometer and strain gauges simultaneously. This approach enabled the measurement of strain throughout the tensile process, providing experimental values for the material's elastic modulus. The results of the experimental values are depicted in Figure 7, revealing that the cooling method has a minimal impact on GFRP within the temperature range of 100 °C to 200 °C, with a variation in no more than 7.3%. However, at 250 °C, water cooling displays the most substantial decrease in elastic modulus, showing a reduction in up to 50% compared to the other cooling methods. This observation implies that water cooling induces the softening of the resin matrix from a rubbery state during the cooling process, thereby influencing the stiffness of GFRP.

The values obtained from a nonlinear fit based on the Boltzmann function closely align with those presented in Figure 7. The regression analysis of the relationship between the elastic modulus residual factor and temperature is as follows:

$$y = \frac{A_1 - A_2}{1 + e^{(x - x_0)/k}} + A_2 \tag{4}$$

Since this paper investigates the relationship between elastic modulus residual factor and temperature, A_1 is the initial value of the elastic modulus discount factor; A_2 is the final value of the elastic modulus discount factor; x_0 is the median temperature of the discount factor; k is the transformation rate of the discount factor; y is the discount factor of the elastic modulus; x is the temperature. To find the coefficient k, divide both sides of Equation (1) by the natural logarithm, Equation (1) becomes:

$$(x - x_0)/k = \ln(A_1 - A_2) - \ln(y - A_2) \tag{5}$$

The coefficients A_1, A_2, x_0 under different cooling methods can be determined from Figure 10, which shows the relationship between the residual factor of elastic modulus and temperature. The results are shown in Table 5. The coefficient k can be obtained by mathematical derivation, which ultimately leads to the equations described by Equations (6)–(8). Air cooling: k_a = 18.84, foam cooling: k_f = 21.17, water cooling: k_w = 15.86.

Air cooling:

$$y_a = \frac{0.86}{1 + e^{(x-266.08)/18.84}} + 0.22 \tag{6}$$

Fire foam cooling:

$$y_f = \frac{0.80}{1 + e^{(x-260.76)/21.17}} + 0.21 \tag{7}$$

Water cooling:

$$y_w = \frac{0.85}{1 + e^{(x-241.42)/15.86}} + 0.15 \tag{8}$$

Figure 10 compares the predicted characteristics of the elastic modulus residual factor temperature with the actual test results. The model's predictions align well with the experimental data, demonstrating the accuracy of the model in forecasting the modulus of elasticity residual factor of GFRP after three cooling methods at various target temperatures.

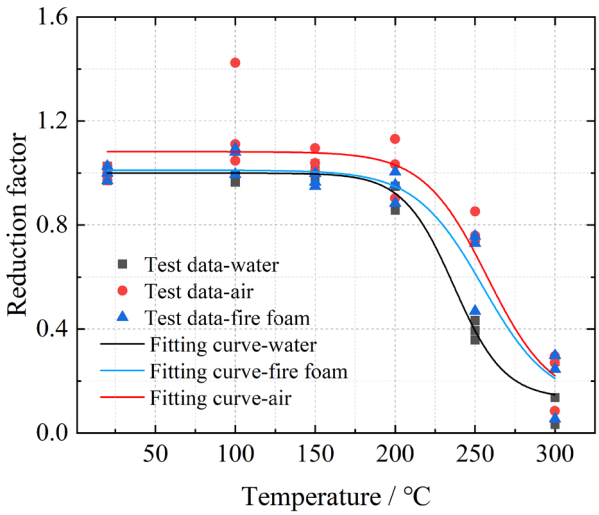

Figure 10. Elastic modulus reduction factors of fire and cooling-affected GFRP.

Table 5. Parameters of Boltzmann model under different cooling modes.

Cooling Method	A_1	A_2	x_0
Air cooling	1.08	0.22	266.08
Fire foam cooling	1.01	0.21	260.76
Water cooling	1.00	0.15	241.42

4.2. Johnson−Cook Model

The original Johnson–Cook (JC) constitutive model [35] can describe the stress–strain relationships under the influence of temperature or strain rate. It is usually considered one of the representative constitutive models due to its simple form and satisfactory performance. Therefore, this model was chosen as the basis for this study. The original model is:

$$\sigma(\varepsilon^p, \dot{\varepsilon}, T) = \left[A + B(\varepsilon^p)^n\right]\left[1 + C\ln\left(\frac{\dot{\varepsilon}}{\dot{\varepsilon}_0}\right)\right]\left[1 - \left(\frac{T - T_R}{T_m - T_R}\right)^m\right] \quad (9)$$

A is the nominal yield stress (MPa) in the tensile process at room temperature, denotes the yield strength of the material, n is the strain hardening parameter, and B is the strain hardening constant (MPa), which can be determined by the fitting method [36]. $\dot{\varepsilon}$, $\dot{\varepsilon}_0$, T, T_R and T_m are the current strain rate, reference strain rate, current temperature, reference temperature, and melting temperature, respectively.

4.2.1. Parametric Analysis

The reference temperature: T_R = 293 K, the reference strain rate: $\dot{\varepsilon}_0$ = 0.005 s^{-1}, A = 12.51 MPa, T_m = 953 K, and T = 373 K. Since strain rate and temperature are not variables in this experiment, Equation (9) can be split into:

$$\sigma(\varepsilon) = A + B\varepsilon^n \quad (10)$$

Converting both sides of the equal value of Equation (10) and dividing them by the natural logarithm gives the following equation:

$$\ln(\sigma(\varepsilon) - A) = n\ln\varepsilon + \ln B \quad (11)$$

After substituting the stress and strain values into Equation (11) for a linear fit, the relationship between lnε and ln($\sigma - A$) under different cooling methods is shown in Figure 11, where n and ln$B$ denote the slope and initial value of the fitted curve, respectively. From this, the coefficients n, and B are calculated in Table 4.

After obtaining the coefficients n, and B for different cooling methods, Equation (9) is transformed into:

$$\frac{\sigma(\varepsilon)}{(A + B\varepsilon^n)} = 1 + C\ln\left(\frac{\dot{\varepsilon}}{\dot{\varepsilon}_0}\right) \quad (12)$$

As shown in Figure 11, the strain values and strain rates derived from the different cooling methods are brought into Equation (12) for a linear fit, where C denotes the slope of the fitted curve, from which the coefficient C can be calculated.

After the linear fit, the values of C for different cooling methods can be known from Figure 12. To find the parameter m, Equation (13) is changed to:

$$\ln\left[1 - \frac{\sigma(\varepsilon)}{A + B\varepsilon^n}\right] = m\ln\left(\frac{T - T_R}{T_m - T_R}\right) \quad (13)$$

As shown in Figure 13, by bringing the numbers of strains and target temperatures from this test into Equation (13) and then performing a linear fit, m can be yielded, as shown in Table 6.

Table 6. Parameters of Johnson–Cook model under different cooling modes.

Parameters	Air Cooling	Fire Foam Cooling	Water Cooling
n	1.16	1.04	1.10
B	5653.33	4105.16	4865.87
C	0.26	0.30	0.38
m	4.26	3.60	3.49

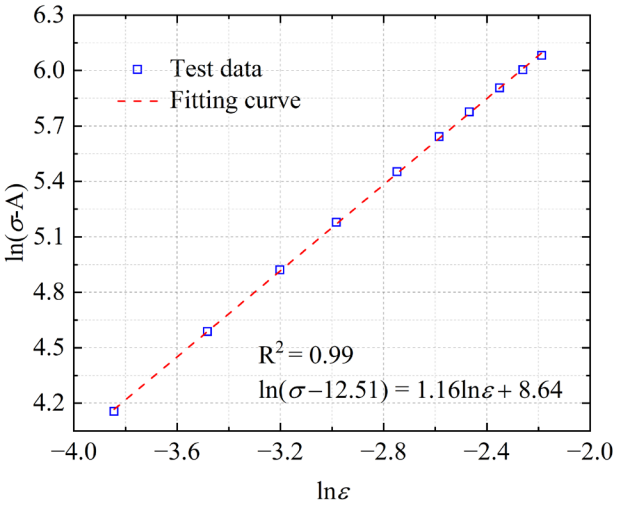

(**a**) Air cooling

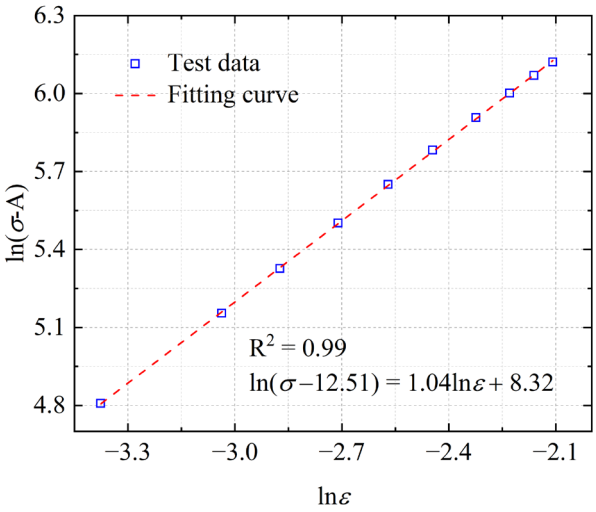

(**b**) Fire foam cooling

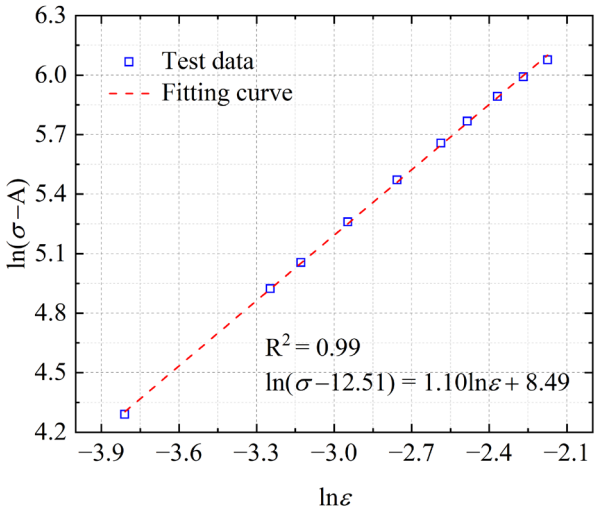

(**c**) Water cooling

Figure 11. The relationship of lnε and ln($\sigma - A$).

Finally, the relationship between stress (σ), strain (ε), deformation temperature (T), and deformation rate was established based on the JC constitutive model. The modified equation T_0 was obtained through linear fitting, resulting in the predicted model data closely aligning with the actual observations.

Fire foam cooling:

$$T_0 = (0.13T - 12.56)\varepsilon + (6.17 \times 10^{-5}T^2 - 0.018T + 6.18 \times 10^{-3})\varepsilon^2 + 10.33 \quad (14)$$

$$\sigma(\varepsilon^p, \dot{\varepsilon}, T) = \left(12.51 + 4105.16\varepsilon^{1.04}\right)\left[1 + 0.30\ln\left(\frac{\dot{\varepsilon}}{0.005}\right)\right]\left[1 - \left(\frac{T-293}{660}\right)^{3.60}\right] - (0.13T - 12.56)\varepsilon - (6.17 \times 10^{-5}T^2 - 0.018T + 6.18 \times 10^{-3})\varepsilon^2 - 10.33 \quad (15)$$

Air cooling:

$$T_0 = \left(1.08 \times 10^{-3}T^2 - 0.32T + 20.76\right)\varepsilon + 8.65 \quad (16)$$

$$\sigma(\varepsilon^p, \dot{\varepsilon}, T) = \left(12.51 + 5653.33\varepsilon^{1.16}\right)\left[1 + 0.26\ln\left(\frac{\dot{\varepsilon}}{0.005}\right)\right]\left[1 - \left(\frac{T-293}{660}\right)^{4.26}\right] - \left(1.08 \times 10^{-3}T^2 - 0.32T + 20.76\right)\varepsilon - 8.65 \quad (17)$$

Water cooling:

$$T_0 = \left(1.07 \times 10^{-3}T^2 - 0.24T + 12.97\right)\varepsilon + \left(-5.12 \times 10^{-4}T^2 + 0.21T - 15.81\right) \quad (18)$$

$$\sigma(\varepsilon^p, \dot{\varepsilon}, T) = \left(12.51 + 4865.87\varepsilon^{1.10}\right)\left[1 + 0.38\ln\left(\frac{\dot{\varepsilon}}{0.005}\right)\right]\left[1 - \left(\frac{T-293}{660}\right)^{3.49}\right] - \left(1.07 \times 10^{-3}T^2 - 0.24T + 12.97\right)\varepsilon - \left(-5.12 \times 10^{-4}T^2 + 0.21T - 15.81\right) \quad (19)$$

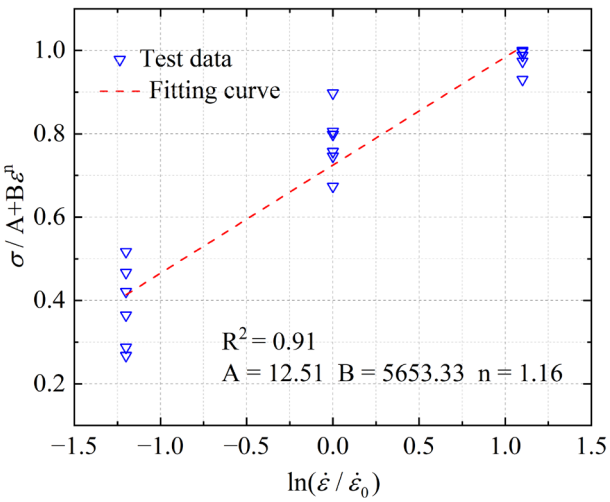

(**a**) Air cooling

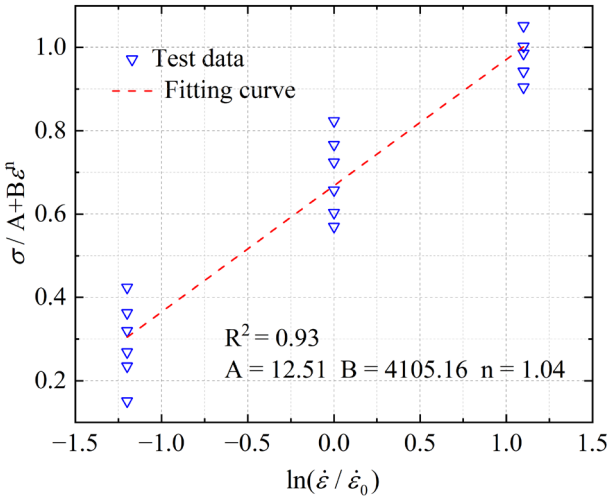

(**b**) Fire foam cooling

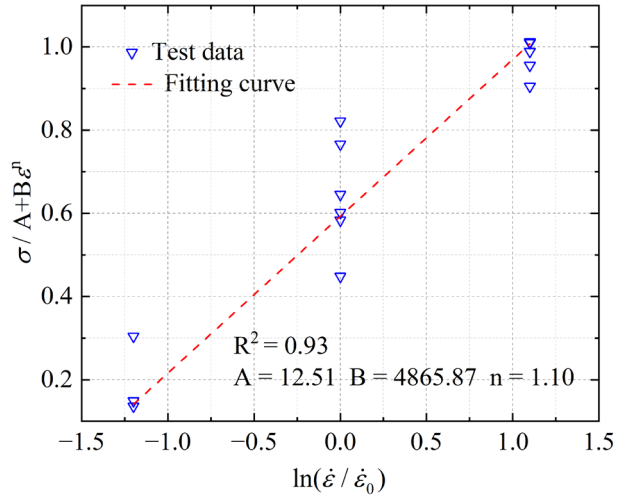

(**c**) Water cooling

Figure 12. The relationship of $\sigma/A + B\varepsilon^n$ and $\ln(\dot{\varepsilon}/\dot{\varepsilon}_0)$.

4.2.2. Verification of the Constitutive Model

The original JC model demonstrates effective predictions at the reference strain rate and temperature. However, given the consideration of mechanical behavior after high-temperature cooling in this experiment, modifications were made to the JC model, resulting in Equations (15), (17) and (19). Figure 14 compares the stress–strain curves obtained from the tests with the predicted data from the modified constitutive model. It can be observed that the predicted equation accurately describes the effects of the three cooling methods on the mechanical behavior of GFRP at different target temperatures. It is important to note that the equation is specifically applicable to the boundary conditions and materials utilized in this study.

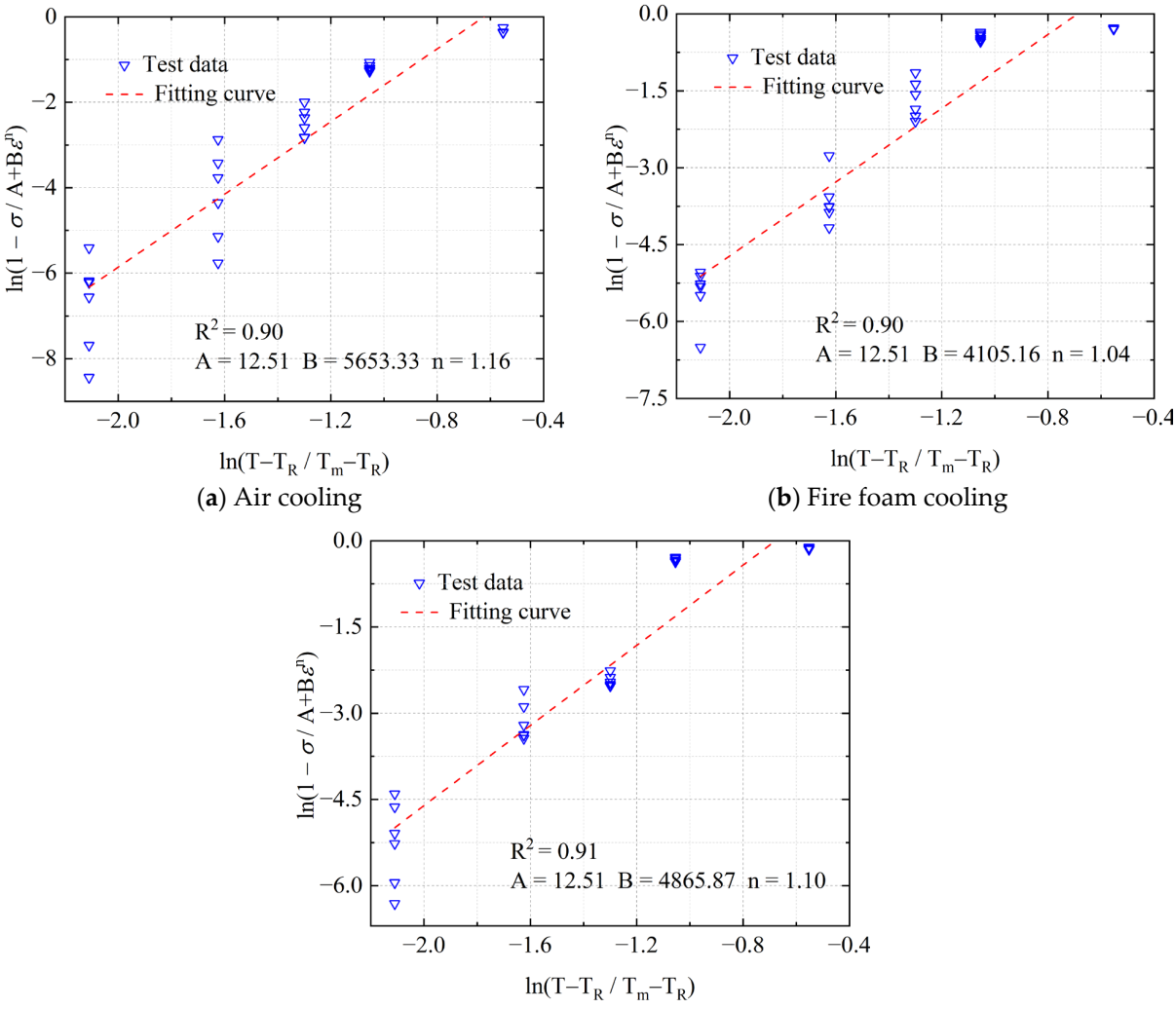

Figure 13. The relationship of $\ln(1-\sigma/A+B\varepsilon^n)$ and $\ln(T-T_R/T_m-T_R)$.

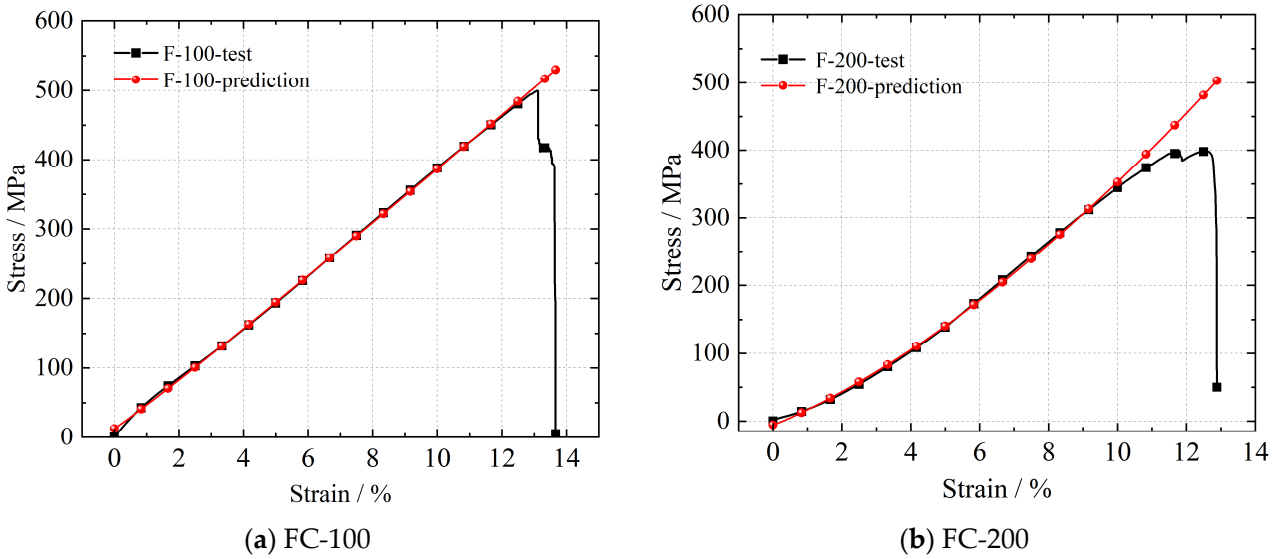

Figure 14. *Cont.*

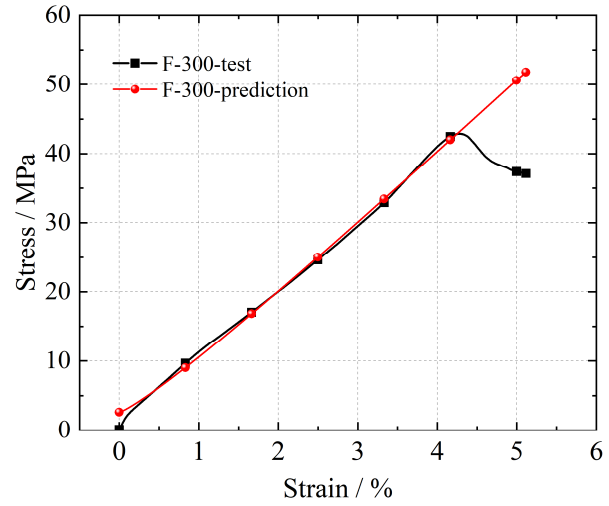

(**c**) FC-300

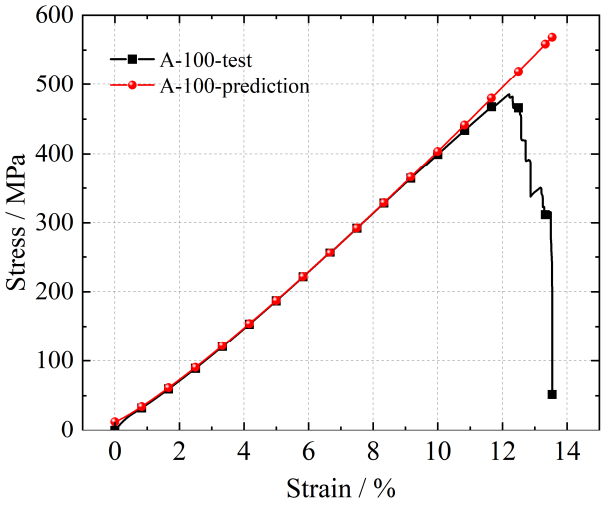

(**d**) AC-100

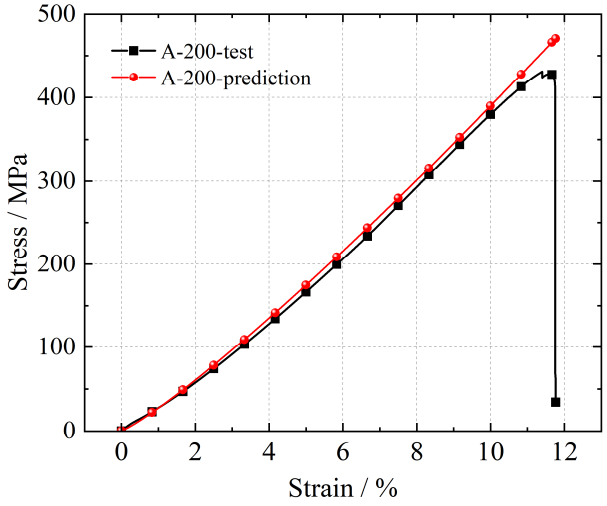

(**e**) AC-200

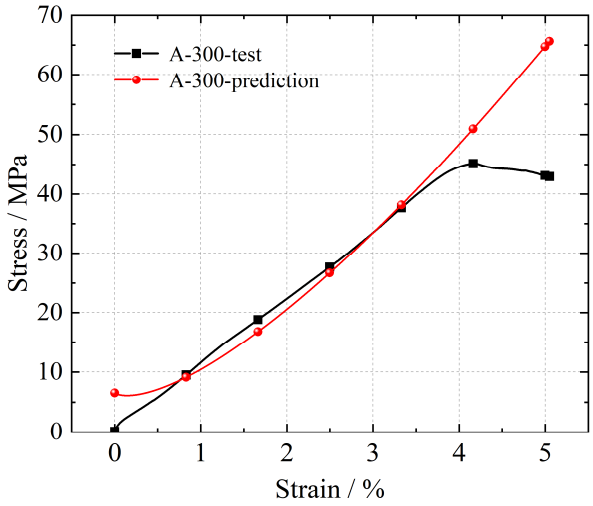

(**f**) AC-300

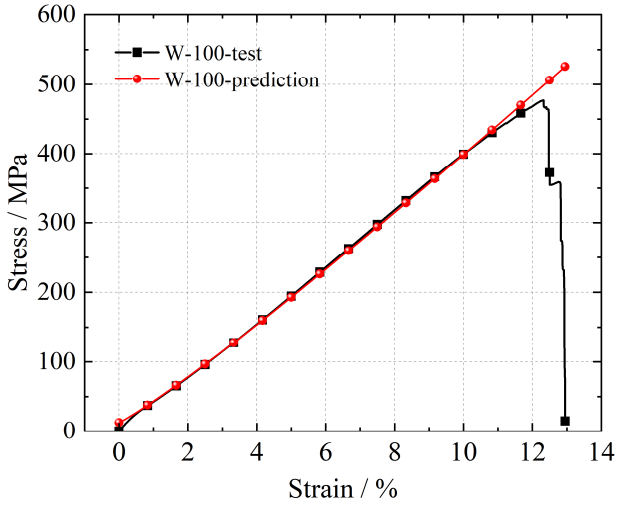

(**g**) WC-100

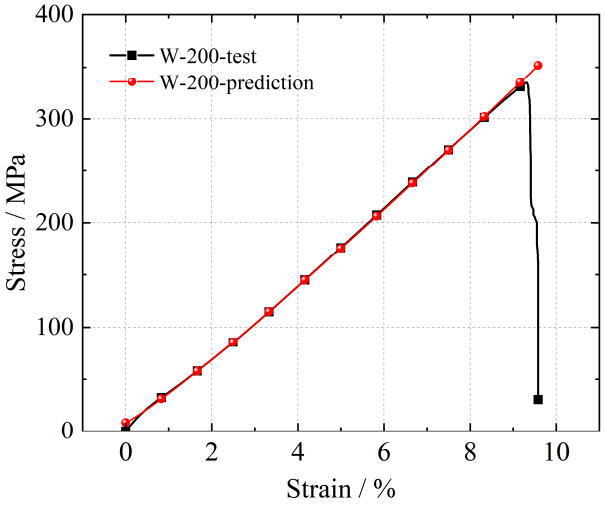

(**h**) WC-200

Figure 14. *Cont.*

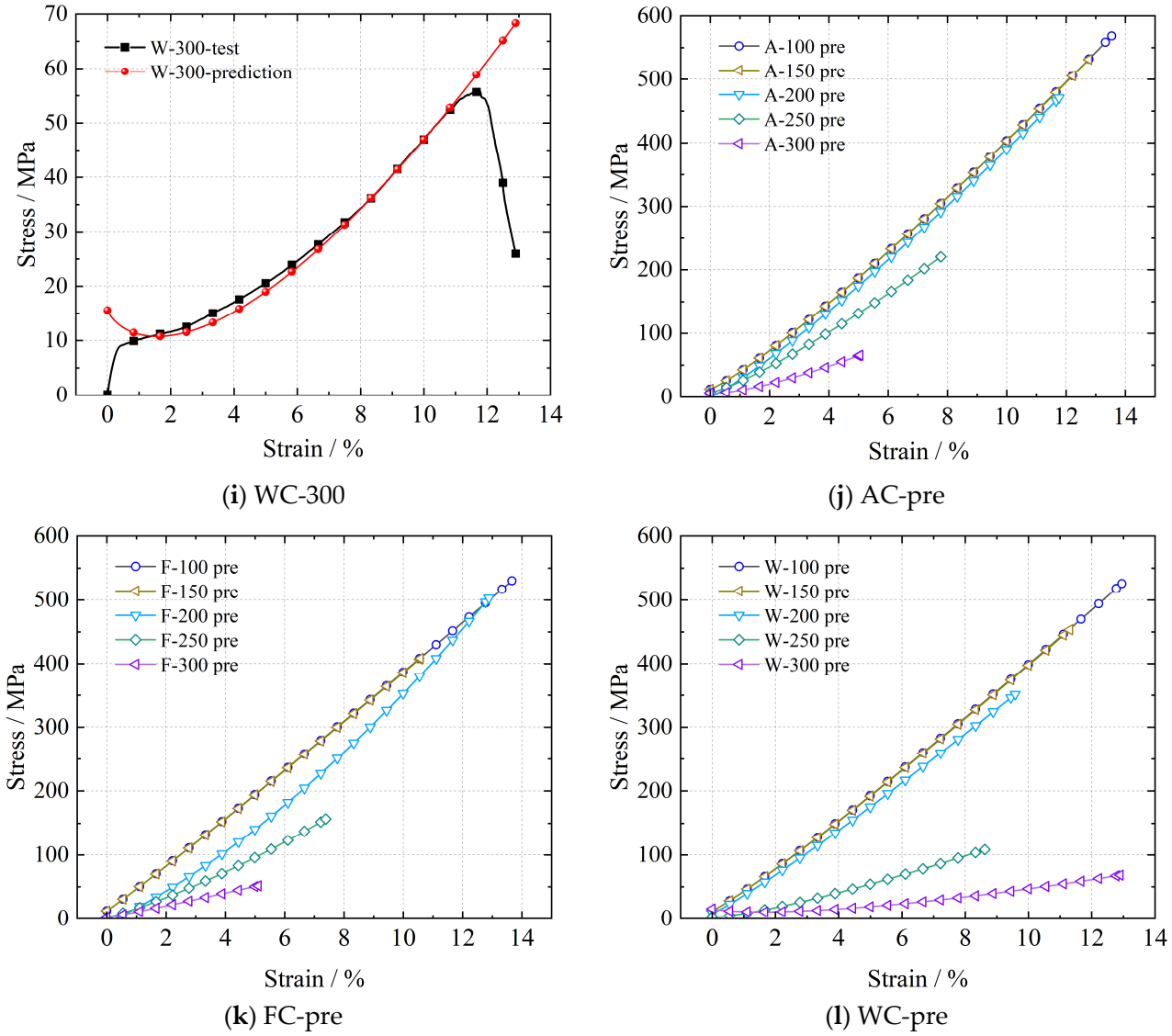

Figure 14. Comparison of predicted and test results.

5. Conclusions

In this paper, the effects of different target temperatures and cooling methods on the tensile properties of GFRP are investigated, and the prediction equations of mechanical properties and theoretical models after high-temperature cooling are derived and verified by experiments. The conclusions of this study are as follows:

1. The elevated temperatures and cooling methods significantly influenced the mechanical properties of GFRP. When exposed to temperatures below 200 °C, the three cooling methods can recover the mechanical properties of GFRP to a greater extent. At temperatures ranging from 20 to 200 °C, the recovery ability of water cooling is the weakest, with tensile strength values of 486.38, 457.30, 405.87, and 328.86. Conversely, natural cooling exhibits the strongest recovery ability, with corresponding tensile strength values of 486.38, 515.24, 485.26, and 428.58; while in 200 °C–300 °C, mechanical properties of GFRP decreased substantially, the ability of the cooling methods to restore the mechanical properties gradually decreased; when at 300 °C, GFRP has basically lost work abilities.
2. The best fire extinguishing method for GFRP materials after exposure to fire is firefighting foam cooling. At 100 °C, the residual factors of elastic modulus (1.05, 1.19) and tensile strength (1.10, 1.06) for GFRP in fire foam cooling and air cooling are greater than those at

ambient temperature. The elastic modulus and tensile strength of GFRP under fire foam cooling and air cooling are greater than those under ambient temperature. They decreased gradually with the increase in temperature. For the same target temperature, the strength retention rates of the materials are air cooling > fire foam cooling > water cooling.

3. The prediction equation of the mechanical properties of GFRP is established based on the experimental results, and the JC constitutive model is also modified to obtain the stress–strain curve equation suitable for this experiment, which is specifically applicable to the boundary conditions and materials utilized in this study.
4. This paper investigates the impact of different firefighting methods on the mechanical properties of GFRP in the event of a fire. Three commonly used cooling methods, namely, fire foam cooling, water cooling, and natural cooling, were employed. This study aims to provide a basis for the post-fire structural safety assessment of buildings.

Author Contributions: Conceptualization, C.Z.; Methodology, C.Z.; Investigation, J.W. and C.Z.; Data curation, J.W.; Writing—original draft, J.W.; Writing—review & editing, C.Z. All authors have read and agreed to the published version of the manuscript.

Funding: This study was supported by the National Natural Science Foundation of China (Grant No. 51868013, 51508482), Sichuan Province Science and Technology Support Program (Grant No. 2022NSFSC0317) and the Natural Science Foundation of Tibet Autonomous (Grant No. XZ202102YD0035C). The authors would like to express their sincere gratitude for their support.

Data Availability Statement: Data are contained within the article.

Conflicts of Interest: The authors declare no conflict of interest.

References

1. Yang, Y.; Fahmy, M.F.M.; Guan, S.; Pan, Z.; Zhan, Y.; Zhao, T. Properties and applications of FRP cable on long-span cable-supported bridges: A review. *Compos. Part B Eng.* **2020**, *190*, 107934. [CrossRef]
2. Chen, Y.; Zhang, C. Stability analysis of pultruded basalt fiber-reinforced polymer (BFRP) tube under axial compression. *Compos. Struct.* **2024**, *327*, 117660. [CrossRef]
3. Zhang, C.; Chen, Y.; Dou, M. Axial Compression Behaviour and Modelling of Pultruded Basalt-Fibre-Reinforced Polymer (BFRP) Tubes. *Buildings* **2023**, *13*, 1397. [CrossRef]
4. Nawaz, W.; Elchalakani, M.; Karrech, A.; Yehia, S.; Yang, B.; Youssf, O. Flexural behavior of all lightweight reinforced concrete beams externally strengthened with CFRP sheets. *Constr. Build. Mater.* **2022**, *327*, 126966. [CrossRef]
5. Li, Y.; Zhang, C. Effects of high-temperature cooling and ultralow cyclic loading on mechanical behavior of Q450 weathering steel. *J. Constr. Steel Res.* **2023**, *202*, 107783. [CrossRef]
6. Zhang, C.; Li, Y.; Wu, J. Mechanical Properties of Fiber-Reinforced Polymer (FRP) Composites at Elevated Temperatures. *Buildings* **2022**, *13*, 67. [CrossRef]
7. Asaro, R.J.; Lattimer, B.; Ramroth, W. Structural response of FRP composites during fire. *Compos. Struct.* **2009**, *87*, 382–393. [CrossRef]
8. Bai, Y.; Keller, T. Modeling of mechanical response of FRP composites in fire. *Compos. Part A Appl. Sci. Manuf.* **2009**, *40*, 731–738. [CrossRef]
9. Wang, Z.; Zhao, X.-L.; Xian, G.; Wu, G.; Raman, R.K.S.; Al-Saadi, S. Effect of sustained load and seawater and sea sand concrete environment on durability of basalt- and glass-fibre reinforced polymer (B/GFRP) bars. *Corros. Sci.* **2018**, *138*, 200–218. [CrossRef]
10. Correia, J.R.; Keller, T.; Garrido, M.; Sá, M.; Firmo, J.P.; Shahid, M.A.; Machado, M. Mechanical properties of FRP materials at elevated temperature—Definition of a temperature conversion factor for design in service conditions. *Constr. Build. Mater.* **2023**, *367*, 130298. [CrossRef]
11. Spagnuolo, S.; Meda, A.; Rinaldi, Z.; Nanni, A. Residual behaviour of glass FRP bars subjected to high temperatures. *Compos. Struct.* **2018**, *203*, 886–893. [CrossRef]
12. Bai, Y.; Keller, T.; Vallée, T. Modeling of stiffness of FRP composites under elevated and high temperatures. *Compos. Sci. Technol.* **2008**, *68*, 3099–3106. [CrossRef]
13. Ashrafi, H.; Bazli, M.; Najafabadi, E.P.; Vatani Oskouei, A. The effect of mechanical and thermal properties of FRP bars on their tensile performance under elevated temperatures. *Constr. Build. Mater.* **2017**, *157*, 1001–1010. [CrossRef]
14. Li, T.; Zhu, H.; Shen, J.; Keller, T. Thermophysical and thermomechanical properties of basalt-phenolic FRP rebars under high temperature. *Constr. Build. Mater.* **2022**, *342*, 127983. [CrossRef]
15. Khorasani, M.; Muciaccia, G.; Consiglio, A.N.; Mostofinejad, D. Evaluating the behavior and bond properties of FRP spike anchors under confined conditions and elevated temperature. *Compos. Struct.* **2023**, *322*, 117407. [CrossRef]

16. Yu, B.; Kodur, V.K.R. Effect of high temperature on bond strength of near-surface mounted FRP reinforcement. *Compos. Struct.* **2014**, *110*, 88–97. [CrossRef]
17. Dong, K.; Hao, J.; Li, P.; Zhong, C. A nonlinear analytical model for predicting bond behavior of FRP-to-concrete/steel substrate joints subjected to temperature variations. *Constr. Build. Mater.* **2022**, *320*, 126225. [CrossRef]
18. Katz, A.; Berman, N. Modeling the effect of high temperature on the bond of FRP reinforcing bars to concrete. *Cem. Concr. Compos.* **2000**, *22*, 433–443. [CrossRef]
19. Faysal, R.M.; Bhuiyan, M.M.H.; Momin, K.A.; Tafsirojjaman, T.; Liu, Y. A review on the advances of the study on FRP-Concrete bond under hygrothermal exposure. *Constr. Build. Mater.* **2023**, *363*, 129818. [CrossRef]
20. Rosa, I.C.; Firmo, J.P.; Correia, J.R.; Mazzuca, P. Influence of elevated temperatures on the bond behaviour of ribbed GFRP bars in concrete. *Cem. Concr. Compos.* **2021**, *122*, 104119. [CrossRef]
21. Xue, Y.-J.; Wang, W.-W.; Wu, Z.-H.; Hu, S.; Tian, J. Experimental study on flexural behavior of RC beams strengthened with FRP/SMA composites. *Eng. Struct.* **2023**, *289*, 116288. [CrossRef]
22. Shayanfar, J.; Kafshgarkolaei, H.J.; Barros, J.A.O.; Rezazadeh, M. Unified strength model for FRP confined heat-damaged circular and square concrete columns. *Compos. Struct.* **2023**, *307*, 116647. [CrossRef]
23. Wang, S.; Stratford, T.; Reynolds, T.P.S. Linear creep of bonded FRP-strengthened metallic structures at warm service temperatures. *Constr. Build. Mater.* **2021**, *283*, 122699. [CrossRef]
24. Cao, V.V.; Vo, H.B.; Dinh, L.H.; Doan, D.V. Experimental behavior of fire-exposed reinforced concrete slabs without and with FRP retrofitting. *J. Build. Eng.* **2022**, *51*, 104315. [CrossRef]
25. Guo, D.; Gao, W.-Y.; Dai, J.-G. Effects of temperature variation on intermediate crack-induced debonding and stress intensity factor in FRP-retrofitted cracked steel beams: An analytical study. *Compos. Struct.* **2022**, *279*, 114776. [CrossRef]
26. Wu, G.; Dong, Z.-Q.; Wang, X.; Zhu, Y.; Wu, Z.-S. Prediction of Long-Term Performance and Durability of BFRP Bars under the Combined Effect of Sustained Load and Corrosive Solutions. *J. Compos. Constr.* **2015**, *19*, 04014058. [CrossRef]
27. Wang, H.; Gong, Z.; Hao, Y.; Deng, Y.; Zhang, C. Evolution of strain-rate dependent compressive failure behavior of ceramifiable FRP composites at high temperature conditions. *Compos. Sci. Technol.* **2023**, *241*, 110145. [CrossRef]
28. Khaneghahi, M.H.; Najafabadi, E.P.; Shoaei, P.; Oskouei, A.V. Effect of intumescent paint coating on mechanical properties of FRP bars at elevated temperature. *Polym. Test.* **2018**, *71*, 72–86. [CrossRef]
29. Wang, Y.C.; Wong, P.M.H.; Kodur, V. An experimental study of the mechanical properties of fibre reinforced polymer (FRP) and steel reinforcing bars at elevated temperatures. *Compos. Struct.* **2007**, *80*, 131–140. [CrossRef]
30. *GB/T 1447-2005*; Fiber-Reinforced Plastics Composites—Determination of Tensile Properties. General Administration of Quality Supervision, and Standardization Administration of the People's Republic of China: Beijing, China, 2005.
31. *GB/T 38515-2020*; The Method for High Temperature Mechanical Properties of Quartz Fabric-Reinforced Resin Matrix Composite Materials. General Administration of Quality Supervision, and Standardization Administration of the People's Republic of China: Beijing, China, 2020.
32. Robert, M.; Benmokrane, B. Behavior of GFRP Reinforcing Bars Subjected to Extreme Temperatures. *J. Compos. Constr.* **2010**, *14*, 353–360. [CrossRef]
33. Li, C.; Yin, X.; Wang, Y.; Zhang, L.; Zhang, Z.; Liu, Y.; Xian, G. Mechanical property evolution and service life prediction of pultruded carbon/glass hybrid rod exposed in harsh oil-well condition. *Compos. Struct.* **2020**, *246*, 112418. [CrossRef]
34. Mazzuca, P.; Firmo, J.P.; Correia, J.R.; Castilho, E. Influence of elevated temperatures on the mechanical properties of glass fibre reinforced polymer laminates produced by vacuum infusion. *Constr. Build. Mater.* **2022**, *345*, 128340. [CrossRef]
35. Johnson, G.R.; Cook, W.H. Fracture characteristics of three metals subjected to various strains, strain rates, temperatures and pressures. *Eng. Fract. Mech.* **1985**, *21*, 31–48. [CrossRef]
36. He, A.; Xie, G.; Zhang, H.; Wang, X. A comparative study on Johnson–Cook, modified Johnson–Cook and Arrhenius-type constitutive models to predict the high temperature flow stress in 20CrMo alloy steel. *Mater. Des.* **2013**, *52*, 677–685. [CrossRef]